Journal of Controlled Release 395 (2026) 115004

Contents lists available at ScienceDirect

Journal of Controlled Release

journal homepage: www.elsevier.com/locate/jconrel

Biodegradable nanofibrous drug-eluting seed for sustained intratumoral immunotherapy☆

Francesco Manfredi [a,b,1], Jingyi Wang [a,c,1], Eleonora Molinari [a,d], Robin Vander Pol [a], Casey Lewis [a], Xinyi Peng [a], Nicola Di Trani [a], Marco Maria Paci [a,b], Danilo Settis [a,b], Madison Alexandra Deeson [a,e], Yongbin Liu [a], Andrew Badachhape [f], Laxman Devkota [f], Michael Ittmann [g], Mahmoud Elsayad [h], Dinh Chuong Nguyen [i], Simbarashe Jokonya [i], Patrick S. Stayton [i], Corrine Ying Xuan Chua [a,*], Alessandro Grattoni [a,j,k,*]

[a] Center of BioNanoengineering, Houston Methodist Research Institute, Houston, TX 77030, USA
[b] College of Engineering, Swansea University, Swansea SA1 8EN, UK
[c] Department of Nuclear Medicine, Shanghai Chest Hospital, Shanghai Jiao Tong University School of Medicine, Shanghai 200025, China
[d] Department of Mechanical and Aerospace Engineering, Polytechnic of Turin, Turin 10129, Italy
[e] Texas A&M University Naresh K. Vashisht College of Medicine, Bryan, TX 77807, USA
[f] Department of Radiology, Baylor College of Medicine, Houston, TX 77030, USA
[g] Department of Pathology and Immunology, Baylor College of Medicine, Houston, TX 77030, USA
[h] Department of Pathology and Laboratory Medicine, McGovern Medical School, Houston, TX 77030, USA
[i] Department of Bioengineering and Molecular Engineering & Science Institute, University of Washington, Seattle, WA, USA
[j] Department of Surgery, Houston Methodist Hospital, Houston, TX 77030, USA
[k] Department of Radiation Oncology, Houston Methodist Hospital, Houston, TX 77030, USA

ARTICLE INFO

Keywords:
B-NDES
Biodegradable polymers
Intratumoral delivery
Triple negative breast cancer
Immunotherapy

ABSTRACT

Intratumoral immunotherapy presents a promising approach for enhancing cancer treatment; however, its effectiveness is limited by heterogeneous intratumoral drug distribution and rapid drug leakage following direct injection. To address these limitations, we developed a biodegradable nanofibrous drug-eluting seed (b-NDES), a reservoir-based implant designed for sustained, localized diffusive delivery of immunotherapeutics. The b-NDES reduces systemic exposure and eliminates the necessity for surgical removal through gradual biodegradation. Implant bodies were fabricated by electrospinning polymeric formulations comprising varying ratios of polycaprolactone (PCL), poly(lactic-co-glycolic acid) (PLGA), and barium sulfate to provide radiopacity. Surface modifications were implemented to adjust the porous structure, allowing for tailored drug elution rates. Comparative comprehensive evaluations of morphology, in vitro release profiles, and degradation kinetics were performed. The optimized 1:4 PCL:PLGA formulation reduced permeable porosity from 18.99 ± 1.26% to 2.74 ± 1.04%, effectively decreasing the rhodamine delivery rate from 162.58 ± 16.11 μg/h to 30.68 ± 11.60 μg/h in vitro. The 1:4 PCL:PLGA structure achieved controlled diffusive drug release profile that extended intratumoral drug persistance in a 4 T1 triple-negative breast cancer (TNBC) murine model, with negligible systemic off-target exposure. Further, long-term degradation studies showed an overall mass loss of 46.32 ± 12.01% at 6 months. When loaded with a combination of CD40 agonist antibody (α-CD40) and a STING agonist (STINGa) and paired with stereotactic radiotherapy, the b-NDES platform achieved complete tumor eradication in 60% of animals. Importantly, no systemic adverse effects were observed with the intratumoral administration of the immunotherapeutic combination via b-NDES. By providing a minimally invasive, sustained-release strategy that naturally degrades to eliminate the need for surgical removal, the b-NDES represents a versatile platform for delivering potent immunotherapeutic combinations against aggressive malignancies.

☆ This article is part of a Special issue entitled: 'CRSingapore 2025' published in Journal of Controlled Release.

* Corresponding authors at: Center for BioNanoengineering, Houston Methodist Research Institute, Houston, TX 77030, USA.
E-mail addresses: ychua@houstonmethodist.org (C.Y.X. Chua), agrattoni@houstonmethodist.org (A. Grattoni).

[1] These authors contribute equally as first authors.

https://doi.org/10.1016/j.jconrel.2026.115004
Received 19 September 2025; Received in revised form 18 February 2026; Accepted 7 May 2026
Available online 12 May 2026

1. Introduction

Immunotherapy has demonstrated survival benefits across several cancer types by relying on the engagement of the body's own immune system to recognize and eliminate cancer cells [1]. In clinical trials, the systemic delivery of immunotherapeutics, such as immune checkpoint inhibitors, has led to promising clinical outcomes [1,2]. However, upon systemic administration, only a small fraction of the administered dose reaches and penetrates the tumor, while the majority circulates throughout the body [3–6]. This widespread systemic exposure limits the therapeutic potential of immunotherapy and is frequently associated with immune-related adverse events (irAEs) [3,7]. Up to 70% of patients receiving PD-1 inhibitors and up to 85% of those treated with CTLA-4 receptor blockade experience irAEs, which, in the most severe cases, require discontinuation of therapy [7–9]. This challenge is further compounded in immune-desert tumors, such as Triple Negative Breast Cancer (TNBC), where systemic immunotherapy shows limited responsiveness due to poor immune infiltration [10]. These limitations highlight the need for more localized delivery strategies that concentrate immunotherapeutics at the tumor site while minimizing systemic dissemination.

Intratumoral administration has emerged as an alternative route for immunotherapy [3,11]. Conceptually, injecting immunotherapeutics directly into the tumor increases drug concentrations at the site, thereby eliciting a strong local immune response [12]. Moreover, this localized approach has the potential to trigger a systemic, tumor-specific response, resulting in the regression of distant tumors [13]. Nonetheless, intratumoral injection still faces challenges, including uneven drug distribution and poor retention due to high tissue density and interstitial pressure and leaky vasculature within tumors [14]. These limitations often necessitate repeated administrations to maintain therapeutic levels, increasing healthcare burden, treatment costs, and the risk of infections [15]. Intratumoral drug delivery strategies require further refinement to fully exploit the therapeutic potential of localized immunotherapy. Among the most commonly employed systems, polymeric nanoparticles and hydrogels have attracted significant attention due to their ease of administration, biodegradable nature, and ability to provide sustained drug release over time [16,17]. However, nanoparticles often exhibit low drug loading efficiency, limiting the payload per unit volume [3,18]. They are also characterized by uncontrolled release profiles and rapid clearance from the tumor site [3,18,19]. Similarly, while hydrogels exhibit superior intratumoral retention, they may display uncontrolled release due to swelling [3,20].

An ideal intratumoral drug delivery platform must be easy to administer in order to minimize patient discomfort and reduce recovery time. It must also be scalable and capable of loading sufficient amounts of drug to achieve the desired therapeutic dose without requiring repeated interventions. The materials used for fabrication could be biodegradable, with a degradation profile tuned to initially preserve the structural integrity of the device. This would allow it to remain at the tumor site and provide controlled, sustained and localized drug release throughout the entire course of treatment. Upon cessation of its drug delivery function, the device would gradually degrade into non-toxic byproducts, eliminating the need for surgical removal, particularly in cases where the tumor has been completely eradicated.

In this study, we present the development of a biodegradable nanofibrous drug-eluting seed (b-NDES) for sustained intratumoral immunotherapy. The term "seed" is used in analogy to brachytherapy seeds, reflecting the small size and minimally invasive implantation of the b-NDES [3], which is designed for sustained intratumoral delivery of immunotherapeutic agents. The b-NDES offers an alternative to a metal-based non-degradable intratumoral drug delivery implant [21–28]. Specifically, we used electrospinning to fabricate a hollow cylindrical structure, which serves as a drug reservoir. The wall is composed of nanofibers that intersect to form fine pores, which enable controlled and sustained drug release. To determine the optimal composition, we characterized four different polymeric formulations of the b-NDES, and evaluated their in vitro release and degradation profile. We demonstrated the ability of b-NDES to provide prolonged intratumoral delivery of CD40 agonist antibody (α-CD40) in an orthotopic 4 T1 TNBC murine model without systemic dissemination. Lastly, we assessed the therapeutic efficacy of the device loaded with α-CD40 and polymeric STING agonist (STINGa) [28,29] in combination with radiotherapy in the same animal model. This combination was selected to reprogram the immune-desert phenotype of TNBC by leveraging STING-mediated innate signaling for dendritic cell activation alongside CD40-driven adaptive T-cell responses [30,31]. These findings highlight the b-NDES as a biodegradable platform for localized, controlled, and sustained drug delivery, ideally suited for combination therapies against aggressive tumors.

2. Materials and methods

2.1. Barium sulfate particle size analysis

Barium sulfate ($BaSO_4$, Sigma-Aldrich) was dispersed (0.1 g) in 10 mL of acetone (Fisher Chemical) to obtain a homogeneous suspension. A drop of the suspension was deposited onto a glass slide and air-dried prior to imaging. Images were acquired using the Olympus BX61 microscope (Center Valley, PA) equipped with a 10×/0.05 non-oil objective and 10× ocular, coupled to an Olympus DP72 digital camera. Particle projected area was measured using an ImageJ-based script, and the equivalent circular diameter was calculated for each particle to obtain the full particle size distribution. The measured mean particle diameter of barium sulfate was 6.07 ± 3.37 nm, and the corresponding particle size distribution is presented in the supplementary information (Fig. S1A).

2.2. Device fabrication

Polycaprolactone (PCL, MW 70,000–90,000 Da) and ester-terminated poly(D,L-lactide-*co*-glycolide) (PLGA, MW 50,000–75,000 Da, lactide:glycolide 85:15) were purchased from Sigma-Aldrich. PCL and PLGA were separately dissolved in acetone (Fisher Chemical) at a concentration of 15% *w/v*. Four formulations were then prepared: (1) PCL, (2) PCL + 0.1 g $BaSO_4$, (3) 1:1 PCL:PLGA +0.1 g $BaSO_4$ (1:1 b-NDES), and (4) 1:4 PCL:PLGA +0.1 g $BaSO_4$ (1:4 b-NDES). Each polymer solution was sonicated for 10 min, stirred overnight for homogeneity, and then electrospun onto a rotating rod collector pre-coated with a sucrose solution. The sucrose solution (45 g of sucrose in 18 mL Milli-Q water) facilitated scaffold detachment. Electrospinning parameters were set to 12 kV, 20 μL/min flow rate, and a 15 cm syringe-to-collector distance, using a 19G syringe needle and a 19G rotating cylindrical collector operated at the lowest available rotation speed (1000 rpm). For each formulation, 6 mL of solution was electrospun onto the collector and dried overnight to ensure complete solvent evaporation. The resulting scaffolds were soaked in Milli-Q water for 5–10 min to dissolve the sucrose layer, then detached, and subsequently transferred to a desiccator (ThermoScientific) for drying. Each scaffold was then cut into 5 mm sections, creating hollow cylindrical devices.

2.3. Surface modification

To reduce porosity and achieve extended drug release, the electrospun devices were subjected to acetone vapor exposure. Devices were mounted on 22G needles and lowered into beakers containing 40 mL of acetone, then sealed with aluminum foil to trap the vapors. Exposure times of 1, 3, 6, or 12 h were tested (Fig. S1); preliminary data indicated that 6 h provided the most favorable balance between fiber fusion and structural preservation; thus, devices used in subsequent studies underwent 6 h of acetone vapor treatment.

2.4. Fiber diameter measurement

Scanning electron microscopy (SEM, Nova NanoSEM 230, Houston Methodist Research Institute, HMRI, Core) was employed to examine cross-sectional and surface morphologies of the devices pre- and post-acetone treatment, as well as after degradation. Samples were sputter-coated with a 7 nm iridium layer and imaged at 5 kV under high vacuum (10^{-3} Pa). Fiber diameter was quantified using ImageJ.

2.5. Surface topography analysis

Devices from each of the four polymeric formulations were sectioned and flattened into membranes, with a subset subjected to acetone vapor treatment prior to analysis. Surface topography was characterized using a Keyence VK-X3000 profilometer, and the resulting images were processed with the Keyence VK-X3000 MultiFileAnalyzer software (version 3.3.1). For every sample, parameters including surface roughness, peak curvature, and developed interfacial area ratio were quantified.

2.6. Porosity quantification

Device dimensions from each of the four formulations, before and after acetone vapor treatment, were measured using a Keyence VK-X3000 profilometer to determine the volume. The devices were then weighed (Mettler Toledo XS105), and density was calculated from the ratio between mass and volume. Porosity (expressed as a percentage) was obtained using the following formula:

$$\text{Porosity}\ (\%) = \left(1 - \frac{\rho}{\rho 0}\right) \text{x}\ 100$$

where ρ is the measured density of the device and ρ0 is the theoretical density of the blend. The latter was calculated for each formulation by weighting the density of each component according to its mass fraction in the mixture. Specifically, the weight ratio of each material was multiplied by its intrinsic density (PCL = 1.145 g/cm^3, PLGA = 1.27 g/cm^3, and $BaSO_4$ = 4.5 g/cm^3), and the resulting values were summed to obtain ρ0.

Open porosity was determined using a diffusion-based release approach with rhodamine as a tracer molecule, comparing untreated devices to devices subjected to 6 h of acetone vapor treatment. Device geometric parameters (outer diameter, inner diameter, wall thickness, and height) were measured using the same profilometer before and after the 6 h of acetone vapor treatment. One end of each device was first sealed using an analog soldering station (APEX Tool Group), and the empty device was weighed. Rhodamine B (Sigma) powder was then introduced into the internal reservoir through the open end using a custom-made funnel, allowing controlled powder insertion and packing within the device. Finally, the remaining open end was sealed using the same soldering station, and the devices were immersed in 2 mL of 1× Phosphate-Buffered Saline (PBS, HyClone). A magnetic stir bar positioned at the bottom of the container ensured continuous mixing of the release medium.

Rhodamine release was monitored using a UV–Vis spectrophotometer (Cary 60, Agilent Technologies) by measuring absorbance at 355 nm every 5 min for up to 30 min. Drug mass released over time was calculated using a calibration curve, and the release rate was obtained as the slope of the linear region of the cumulative mass-versus-time curve. Open porosity was calculated according to the following equation:

$$\text{Open porosity}\ (\%) = \frac{\text{dm}}{\text{dt}}\ \text{x}\ \frac{1}{\text{C0 A}}\ \text{x}\ \frac{\tau\ \text{L}}{\text{D0}}\ \text{x}\ 100$$

where dm/dt is the experimentally determined mass release rate, C0 is the initial rhodamine concentration inside the device, assumed to be equal to the saturation concentration (20 mg/mL), A is the exchange area, defined as the lateral surface area of the device available for mass transport, D0 is the diffusion coefficient of rhodamine in PBS (4.1×10^{-10} m^2/s) [32], L is the effective diffusion path length corresponding to the device wall thickness, and τ is the tortuosity factor (values in porous systems range from ~1 for straight-line transport to >4 in highly convoluted structures). In the absence of direct tortuosity measurements, a value of τ = 2 was assumed, consistent with commonly adopted modeling approaches for transport in porous membranes [33].

2.7. In vitro degradation profile assessment

Devices fabricated from the four formulations and after 6 h of acetone vapor exposure were weighed and placed in 1× PBS at 37 °C and 50 °C. Every seven days, devices were removed from the medium, rinsed with Milli-Q water, vacuum-dried, and re-weighted. Weight loss was calculated using:

$$\text{R} = \frac{\text{W0} - \text{Wt}}{\text{W0}}\ \text{x}\ 100$$

where W0 is the initial dry weight and Wt is the dry weight at each time point. This analysis continued for approximately six weeks, enabling the assessment of early and accelerated degradation behavior.

The degradation experiment was additionally conducted over 3 weeks using 1× PBS adjusted to pH 6.5 (Teknova). The pH of the degradation medium was monitored using a pH meter (Accumet AE150, Fisher Scientific), and the medium was replaced every 7 days to maintain constant pH conditions.

2.8. Animal model and tumor induction

4 T1 breast cancer cells (low passage, gifted by Haifa Shen HMRI) were maintained in RPMI-1640 medium (Gibco) supplemented with L-Glutamine, 25 mM HEPES, 10% fetal bovine serum (FBS), and 1% penicillin/streptomycin. Cultures were incubated at 37 °C in a humidified 5% CO_2 atmosphere, with routine mycoplasma testing to ensure sterility. Six-week-old female BALB/c mice (Taconic Bioscience) were housed at HMRI Comparative Medicine facility under conditions compliant with the National Institutes of Health Guide for the Care and Use of Laboratory Animals and the Animal Care and Use Review Office (ACURO). Mice were monitored daily for overall health, including signs of discomfort, weight change, or abnormal behavior. Orthotopic tumors were induced by injecting 3×10^4 cells in 100 μL of a 3:1 PBS-to-Matrigel mixture into the fourth left mammary fat pad. Tumors were measured thrice weekly with calipers, and mice were randomized into treatment groups when tumor volumes reached about 150 mm^3 using the formula: 0.5 x Length x Width^2. Length represents the longest tumor axis, and Width is perpendicular to the length. Human endpoints were defined as tumor volume ≥ 2000 mm^3 or ulceration. Body weight and temperature was recorded throughout the study to assess systemic toxicity.

2.9. Antibodies and reagents

CD40 monoclonal antibodies (FGK4.5, BE0016, Bio X Cell) were lyophilized without Alexa Fluor labeling for in vitro work, using D-(+)-trehalose dihydrate (Millipore-Sigma, #90210) as a cryoprotectant. The antibody solution was frozen at −80 °C and lyophilized (LABCONCO Freezone 4.5) for 48 h. For in vivo fluorescent tracking, Alexa Fluor 790 (A37569, Invitrogen™) was conjugated to α-CD40, and unbound dye was removed by centrifugation in Amicon Ultracel-30 k filters. Polymeric STING agonist (STINGa) was synthesized according to our previously published protocols [28,29]. The polymeric mannose construct lacking STING (poly-mannose) was conjugated with rhodamine to assess the in vitro release profile of STINGa.

2.10. Intratumoral delivery and longitudinal imaging

α-CD40-AF790 was loaded into b-NDES scaffolds (1:1 vs 1:4 b-NDES). Mice received a single intratumoral implantation, and fluorescence imaging (IVIS Spectrum) was performed on Days 1, 3, 7, 10, 13, and 14. Fluorescence in the tumor region was quantified as total radiant efficiency (p/s/cm^2/sr/μW) to monitor drug retention and release kinetics. At Day 14, organs (tumor, liver, spleen, lungs, kidneys, and lymph nodes) were harvested for ex vivo fluorescence imaging to evaluate biodistribution.

2.11. Ex vivo CT imaging of tumors

Tumors implanted with b-NDES were scanned via micro-CT (Siemens Inveon) at 80 kV, 0.5 mA, and 850 ms exposure time, yielding 960 images of 19.3 μm isotropic resolution. The scan lasted 40 min. CT images enabled tracking of the device location and structural changes.

2.12. In vitro release tests

Devices were exposed to acetone vapor for 6 h, weighed in the empty state, and subsequently loaded with lyophilized α-CD40 and poly-mannose conjugated with rhodamine using the loading procedure described above. Following drug loading, the open ends were sealed, and the devices were placed into custom-made baskets immersed in 2 or 3 mL (depending on the experiment) of 1× PBS. A magnetic stir bar positioned at the bottom of the container ensured continuous mixing of the release medium.

Release studies were conducted for up to 12 days using a UV–Vis spectrophotometer (Cary 60, Agilent Technologies) with absorbance measurements acquired daily at 280 nm and 560 nm. The cumulative drug mass released over time was calculated based on calibration curves generated for each compound.

2.13. Tumor treatment

Radiotherapy (8 Gy/day, 3 consecutive days) was administered before immunotherapy, using the SMART + X-ray Irradiator at the tumor site exclusively. Immediately following the radiation session, b-NDES loaded with a combined dose of α-CD40 and STINGa was implanted. The device contained 250 μg of lyophilized α-CD40 formulation (anti-CD40 + trehalose), corresponding to ~140–150 μg of active antibody (~57% *w/w*); this dose was selected to align with previously reported therapeutically effective in vivo anti-CD40 regimens [26]. In addition, the device was loaded with 250 μg of lyophilized poly-STING, corresponding to ~12–15 μg of active STING moieties (5–6% *w/w* active content). Reported STING regimens in TNBC models typically involve repeated systemic administrations [34]; therefore, the selected dose falls within the same order of magnitude of biologically effective ranges, while being delivered locally through sustained intratumoral release of a mannose-functionalized construct designed to enhance uptake by antigen-presenting cells [29]. The control group received vehicle-only implants, radiation alone, or monotherapy.

2.14. Evaluation of treatment-induced immunological mechanisms

Flow cytometric analysis was performed on 4 T1 tumor samples collected at the day 7 post-treatment. Tumors were harvested immediately after euthanasia, placed in cold RPMI-1640 supplemented with 2% FBS, and processed for single-cell suspension generation. Tumor tissues were finely minced into approximately 1–2 mm fragments and enzymatically digested in RPMI-1640 containing 1× collagenase/hyaluronidase (Stemcell technologies) and DNase I (MedChemExpress) for 30 min at 37 °C under agitation (200–300 rpm). Enzymatic activity was quenched by adding an equal volume of RPMI-1640 supplemented with 10% FBS, and the resulting cell suspension was filtered through 70 μm cell strainers to remove undigested debris. Cells were centrifuged at 500 *g* for 5 min at 4 °C, and red blood cells were lysed using ACK lysis buffer (Quality Biological). Following lysis, cells were washed and resuspended in FACS buffer (PBS supplemented with 2% FBS and 2 mM EDTA). Viable cells were counted using Trypan Blue (Gibco) exclusion and aliquoted at 1×10^6 cells per sample into 96-well V-bottom plates for staining. Cells were first incubated with a fixable viability dye for 30 min at room temperature in the dark. After washing, Fc receptors were blocked using anti-CD16/CD32 antibody (BioLegend, Cat# 101302, USA) for 10 min at 4 °C. Without further washing, cells were stained with CD45-Brilliant Violet 421 (BioLegend, Cat# 103134, USA), CD3e-PE (BioLegend, Cat# 100308, USA), CD4-Brilliant Ultraviolet 737 (BD Biosciences, Cat# 612843, USA), CD8a-PerCP-Cy5.5 (BioLegend, Cat# 100734, USA), CD11b-PE (BioLegend, Cat# 101208, USA), CD11c-Brilliant Violet 786 (BD Biosciences, Cat# 563735, USA), F4/80-FITC (BioLegend, Cat# 123108, USA), Mannose Receptor-PE-Cy7 (E Biosciences, Cat# 25206182, USA), CD86-Brilliant Ultraviolet 805 (BD Biosciences, Cat# 741946, USA), MHC II-PerCP-eFluor 710 (Thermo Fisher Scientific, Cat# 46532182, USA), CD103-Alexa Fluor 647 (BioLegend, Cat# 127641, USA), Ly-6C-Brilliant Violet 480 (BD Biosciences, Cat# 569438, USA) and Ly-6G-Brilliant Violet 650 (BioLegend, Cat# 127641, USA) for 30 min at room temperature in the dark. Following staining, cells were washed with FACS buffer and resuspended in FACS buffer for acquisition. Samples were acquired on a BD Symphony A5SE flow cytometer and analyzed using FlowJo software (v10.8.0). Compensation was performed using single-stained compensation beads, and fluorescence minus one controls were included for selected markers when required.

2.15. Serum cytokine and chemokine analysis by Luminex

Peripheral blood was collected from tumor-bearing mice at Day 7 post-treatment, allowed to clot, centrifuged (5000 *g*, 12 min, 4 °C), and serum was aliquoted and stored at −80 °C. Serum was transferred to low-protein-binding tubes, aliquoted to avoid repeated freeze–thaw cycles, and stored at −80 °C until analysis. Serum cytokines and chemokines were quantified using a magnetic bead–based multiplex assay (MILLIPLEX® Mouse Cytokine/Chemokine Magnetic Bead Panel, MilliporeSigma, Cat. No. MCYT1-190 K-04) according to the manufacturer's instructions. Serum samples were thawed on ice, gently mixed, and diluted 1:2 in the assay buffer. Standards were prepared by serial dilution to generate an 8-point standard curve. Diluted samples and standards were incubated with antibody-coated magnetic beads overnight at 4 °C on a plate shaker, followed by three wash steps using a magnetic separator. Plates were then incubated sequentially with biotinylated detection antibodies and streptavidin–phycoerythrin. Beads were resuspended in sheath fluid and acquired on a Luminex platform using xPONENT software (Luminex Corporation), with a minimum of 50 beads collected per analyte per well. Instrument calibration and performance verification were performed according to the manufacturer's recommendations prior to acquisition. Cytokine concentrations were calculated from standard curves using a five-parameter logistic (5-PL) regression model implemented in xPONENT software. The analytes quantified in this study included IL-6, IL-10, CXCL10 (IP-10), and TNF-α.

2.16. Analysis of metastatic burden and liver toxicity

At the study endpoint, lungs and livers were harvested, fixed in 10% neutral-buffered formalin, embedded in paraffin, sectioned at 5 μm, and H&E stained (HMRI Research Pathology Core). H&E images were acquired using an Olympus BX61 microscope. A board-certified pathologist, blinded to treatment, scored liver inflammation. Perivascular inflammation was assessed using a 0–3 scale, where 0 = no inflammation, 1 ≤ 30%, 2 = 30–60%, and 3 ≥ 60% of vessels involved. Lobular inflammation was evaluated by counting the number of foci, defined as clusters of more than four inflammatory cells not associated with

vessels, in five randomly selected 200× microscopic fields. Spontaneous lung metastases was quantified using ImageJ.

2.17. Blood chemistry analysis

Serum was collected at the study endpoint and submitted to the Center for Comparative Medicine at Baylor College of Medicine for blood chemistry analysis.

2.18. In vivo degradation profile assessment

Six devices were implanted subcutaneously in the dorsal region of 10-week old female Balb/c mouse. In vivo micro-computed tomography (CT) scans imaging was conducted at baseline (month 0) and at 2 and 4 months post-implantation to longitudinally monitor device integrity and radiopacity. Imaging at 6 months could not be performed due to temporary instrument unavailability. Scans were acquired using a micro-CT system (MR Solutions CT80, MR Solutions Ltd., UK) at a tube voltage of 40 kVp and a tube current of 0.5 mA with a flat-panel detector operated in 1 × 1 binning mode. Images were reconstructed at an isotropic voxel size of 200 μm. The reconstructed datasets were analyzed to extract the maximum Hounsfield Unit (HU Max) values of each device for quantitative evaluation of radiopacity over time. HU Max represents the highest attenuation value measured within a defined region of interest on a CT image, corresponding to the most radiodense structure present in that region. At predefined time points (2, 4, and 6 months post-implantation), devices were explanted. Upon retrieval, a subset of devices was collected with the surrounding skin tissue intact, while the remaining devices were isolated by enzymatic digestion using a 1× collagenase solution, followed by thorough rinsing with Milli-Q water. Explanted devices were subsequently vacuum-dried and weighed, and mass loss was calculated using the equation described above. The retrieved devices were further subjected to surface topographical analysis using the previously described profilometric microscope. For each sample, parameters including surface roughness and developed interfacial area ratio were quantified.

2.19. Ex vivo CT imaging of devices

Implantable devices from the control, month 2, month 4, and month 6 groups were scanned on a mouse body platform on a nanoScan PET/CT scanner (Mediso, Budapest, Hungary). All sixteen samples were held in centrifuge tubes and imaged in the same field of view in a single scan. CT images were acquired at 62 μm isotropic resolution. Image parameters were as follows: X-ray voltage 70 kVp, exposure 400 ms, X-ray current 500 μA, 1440 projections, binning 1:1, dose 25 cGy, and scan time 11 min. Images were viewed and processed using Horos (Horos Project, New York, USA). Maximum intensity projections (MIP) were generated with 5-slice slabs in the coronal direction to create volumes for each device. Devices appeared radio-opaque with higher signal relative to centrifuge tubes, enabling manual segmentation of device volumes in Horos. A region-of-interest (ROI) was drawn using the brush tool on contiguous slices for each volume to segment the device and determine volumes (mm^3) and mean Hounsfield Unit (HU) values. HU values were interpreted relative to air (−1000 HU) as reference; therefore, negative values may occur in low-density components.

2.20. Evaluation of device biocompatibility

b-NDES with the surrounding skin samples from the in vivo biodegradation study were fixed in 10% neutral-buffered formalin, embedded in paraffin, sectioned at 5 μm, and stained with either hematoxylin and eosin (H&E) or Masson's trichrome at the HMRI Research Pathology Core. Histological images were acquired using the Olympus BX61 microscope and used for subsequent qualitative and quantitative analyses. H&*E*-stained sections were independently and blindly evaluated by a board-certified pathologist according to predefined histopathological scoring criteria (Tables 1–3) to assess local tissue response and biocompatibility. Masson's trichrome–stained sections were used specifically for the quantitative assessment of fibrotic capsule formation. Fibrotic capsule thickness surrounding the implanted devices was measured using ImageJ software on digitally acquired histological images. For each sample, ten independent measurements were collected and averaged to obtain the final quantitative value.

2.21. Statistical analysis

Data are presented as mean ± Standard Deviation (SD) or Standard Error of the Mean (SEM). Statistical significance was determined via GraphPad Prism using unpaired *t*-tests, one-way ANOVA, or two-way ANOVA with standard post-hoc analyses. A p-value <0.05 was considered significant, significance levels are * = $p < 0.05$; ** = $p < 0.01$; *** = $p < 0.001$; **** = $p < 0.0001$. Absence of annotation indicates no significant difference.

3. Results and discussion

3.1. Fabrication and morphology of a biodegradable nanofibrous device (b-NDES)

Our laboratory previously developed the NDES, an intratumoral drug delivery implant composed of a stainless-steel reservoir with nanofluidic silicone membrane [21–28]. While effective, its metallic structure was conceived for applications whereby upon drug delivery termination, the implant would be retrieved together with the surgical resection of the tumor. For non-resectable tumors or for tumors for which resection is not recommended, we created a biodegradable implant technology (b-NDES) that preserves the dimensions and functional properties of its predecessor while naturally degrading over time. This advancement eliminates the need for device retrieval, thereby expanding the clinical applicability of the intratumoral implant approach.

We selected polycaprolactone (PCL) and poly(lactic-*co*-glycolic acid) (PLGA) to fabricate the b-NDES. PCL and PLGA are FDA-approved biodegradable polymers with distinct degradation kinetics: PLGA degrades rapidly, whereas PCL offers greater mechanical stability [35]. Four different formulations of the b-NDES were evaluated for mechanical stability, morphology, controlled release and degradation kinetics. The formulations are: PCL, PCL + $BaSO_4$, 1:1 PCL:PLGA + $BaSO_4$ (1:1 b-NDES), and 1:4 PCL:PLGA + $BaSO_4$ (1:4 b-NDES). By blending PCL and PLGA, we aimed to tailor the degradation profile in order to achieve complete resorption within approximately one year [35]. To confer radiopacity and enable visualization via CT imaging for real-time

Table 1
Cell type/response histological evaluation.

	Score				
Cell type/response	0	1	2	3	4
Polymorphonuclear cells	0	Rare (1–5/hpf)	Mild to moderate (5–50/hpf)	Heavy infiltate	Packed
Lymphocytes	0	Rare (1–5/hpf)	Mild to moderate (5–50/hpf)	Heavy infiltate	Packed
Plasma cells	0	Rare (1–5/hpf)	Mild to moderate (5–50/hpf)	Heavy infiltate	Packed
Macrophages	0	Rare (1–5/hpf)	Mild to moderate (5–50/hpf)	Heavy infiltate	Packed
Gian cells	0	Rare (1–5/hpf)	Mild to moderate (5–50/hpf)	Heavy infiltate	Sheets
Necrosis	0	Minimal	Mild	Moderate	Severe

Table 2
Response histologicl evaluation.

Response	Score				
	0	1	2	3	4
Neovascularization	0	Minimal capillary proliferation, focal, 1–3 buds	Groups of 4–7 capillaries with supporting fibroblastic structures	Broad band of capillaries with supporting fibroblastic structures	Extensive band of capillaries with supporting fibroblastic structures
Fibrosis	0	Narrow band	Moderately thick band	Thick band	Extensive band
Fatty Infiltration	0	Minimal fat associated with fibrosis	Several layers of fat and fibrosis	Elongated and broad accumulation of fat cells around implant sites	Extensive fat completely surrounding the implant

Table 3
Test article categorization.

Reactivity grade	Test article relative score
Minimal or no reaction	0.0–2.9
Slight reaction	3.0–8.9
Moderate reaction	9.0–15.0
Severe reaction	>15

monitoring in a non-invasive manner, we incorporated $BaSO_4$. We used electrospinning to fabricate the b-NDES, as it can produce finely porous structures from polymer solutions, a crucial feature for achieving controlled and prolonged drug release [36].

Each formulation was dissolved in acetone and electrospun onto a rotating cylindrical collector, forming a hollow scaffold with porous walls composed of nanofibers. The resulting structure was then sectioned into 5 mm-long cylinders with an outer diameter of 1.49 ± 0.05 mm, creating the biodegradable NDES (Fig. 1A-B). It is designed to be compatible with existing clinical trocar implantation used for brachytherapy seeds insertion. The hollow central reservoir has an estimated capacity of approximately 2 mg for drug-loading.

Optical inspection confirmed uniform cylindrical structures with a hollow core of 1.17 ± 0.03 mm inner diameter (Fig. 1B-C). Cross-sectional SEM of the b-NDES showed well-defined hollow morphologies (Fig. 1C), while higher-magnification images revealed a nanofiber network with submicron diameters (Fig. 1D). PCL alone had an average fiber diameter of 0.25 ± 0.16 μm, whereas the addition of $BaSO_4$ increased it to 0.45 ± 0.12 μm (Fig. 1E). The 1:1 b-NDES had an average diameter of 0.23 ± 0.06 μm, whereas the 1:4 b-NDES fibers measured 0.45 ± 0.23 μm. These results showed that refining electrospinning conditions led to uniform fiber formation and structural integrity across all formulations.

3.2. Surface modification and impact on drug diffusion

To further regulate the release rate, devices were exposed to acetone vapor to induce partial fiber fusion, thereby decreasing pore size and limiting diffusion. The 6 h exposure yielded the optimal balance between structural integrity and reduced porosity (Fig. S1B-E). SEM revealed that the PLGA-rich formulation (1:4 b-NDES) had more pronounced fiber fusion, creating fewer and smaller surficial pores (Fig. 2A). Profilometry further confirmed these observations, offering an indirect assessment of reduced two-dimensional porosity (Fig. 2B-C). Among all formulations, only the 1:4 b-NDES showed significant topographical changes, where the reduction in peak height, peak sharpness, valley depth, and interfacial complexity produced a smoother, more compact surface with fewer voids (Fig. 2D-F). The porosity of the 1:4 b-NDES decreased from 93.55 ± 0.66% to 83.25 ± 2.89% after acetone vapor exposure (Fig. 2G). Notably, prior to treatment, only 18.99 ± 1.26% of the porosity was open and accessible to diffusion, which was further reduced to 2.74 ± 1.04% following acetone exposure (Fig. 2H). This pronounced reduction in open porosity provides a mechanistic explanation for the drastic change observed in rhodamine transport kinetics, where the delivery rate decreased from 162.58 ± 16.11 μg/h to 30.68 ± 11.60 μg/h, yielding a slower and more sustained release profile (Fig. 2I–J), compared to 1:1 b-NDES. These findings demonstrated that acetone vapor exposure can fine-tune scaffold architecture to extend the drug release profile while preserving mechanical integrity of the device.

3.3. In vitro degradation profile of the biodegradable device

We evaluated long-term scaffold degradation in PBS at 37 °C and 50 °C. Evaluating degradation at 50 °C allows for the evaluation of degradation kinetics within an accelerated timeframe, without compromising the integrity of the polymeric structure. SEM analyses over four weeks showed minimal morphological changes at 37 °C (Fig. 3A), whereas accelerated degradation at 50 °C revealed more polymeric matrix breakage, especially in the 1:4 b-NDES (Fig. 3B). Quantitative weight measurements (Fig. 3C) confirmed that formulations containing PLGA degrade faster at 50 °C, with a particularly significant temperature effect observed in the 1:4 b-NDES ($p < 0.0001$), as the devices had disintegrated into small fragments on day 42. At 37 °C, the monthly mass loss was measured at 0.68 ± 0.74% for pure PCL, 0.59 ± 2.94% for PCL + $BaSO_4$, 4.51 ± 2.68% for the 1:1 b-NDES formulation, and 1.7 ± 1.62% for the 1:4 b-NDES formulation (Fig. 3D). In contrast, at 50 °C, the 1:4 b-NDES formulation exhibited the highest monthly degradation rate, with a mass loss of 75.41 ± 1.78%. This value was significantly higher ($p < 0.0001$) than all the other formulations, with monthly degradation rate measured at 2.19 ± 2.34% for PCL, 3.28 ± 2.28% for PCL + $BaSO_4$, and 43.33 ± 4.43% for the 1:1 b-NDES. These results reflect the lower stability of PLGA compared to PCL, with higher PLGA content accelerating degradation [37,38]. While PLGA degrades slowly at first due to limited water penetration, accumulated acidic byproducts (e.g., lactic and glycolic acid) eventually trigger autocatalytic bulk degradation, consistent with known behavior of similar PLGA formulations [38]. As a consequence, the polymer composition of the device is expected to progressively evolve during degradation, with preferential PLGA erosion leading to a gradual shift in the effective PCL: PLGA ratio.

To further validate these findings under tumor-like conditions, degradation studies were repeated in an acidic environment mimicking the tumor microenvironment (pH 6.5). Under these conditions, degradation of 1:4 b-NDES proceeded more rapidly than at physiological pH, as PLGA degrades faster at lower pH due to accelerated ester bond hydrolysis [38]. At 50 °C, degradation was faster than at 37 °C, with the device fully degrading within three weeks (Figure E). At 37 °C, no appreciable pH changes were detected. In contrast, under accelerated conditions (50 °C and pH 6.5), significant pH variations were observed at days 14 and 21 ($p < 0.0001$ and $p < 0.001$), consistent with enhanced PLGA degradation and accumulation of acidic byproducts (Fig. 3F).

Importantly, degradation kinetics did not interfere with the drug release profile, which remained well-regulated. Despite the enhanced PLGA content, 1:4 b-NDES still maintained structural integrity during the crucial initial weeks, enough to sustain drug release, yet gradually biodegraded without requiring device retrieval.

Thus, the 1:4 b-NDES formulation emerged as optimal for intratumoral applications, offering initial stable implantation, controlled payload release, and eventual scaffold breakdown. Our findings identify the 1:4 b-NDES formulation as the optimal composition for intratumoral

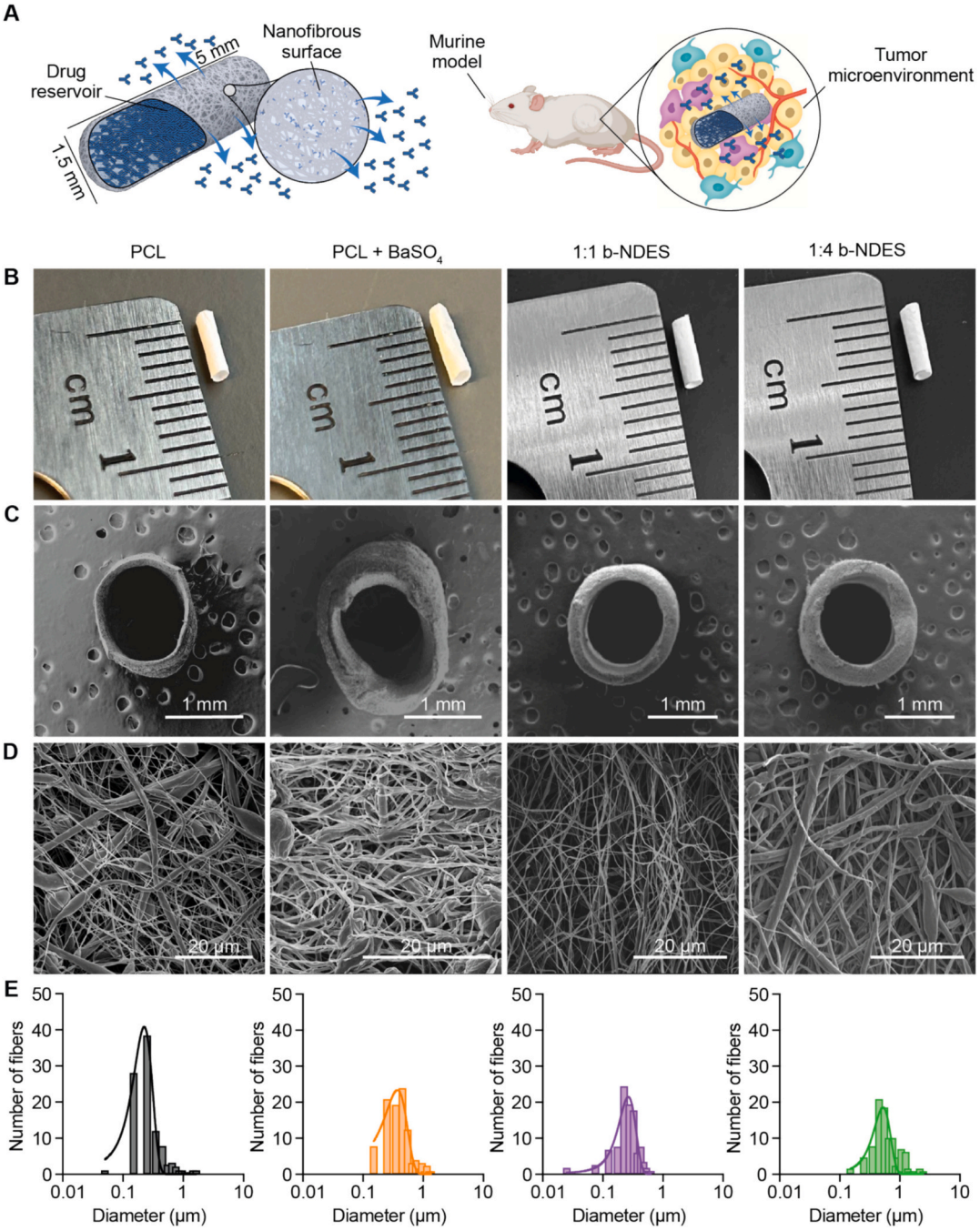

Fig. 1. Morphological characterization and structural analysis of devices with different formulations, including PCL, PCL + $BaSO_4$, 1:1 b-NDES, and 1:4 b-NDES. (A) Schematic representation of the b-NDES, illustrating the drug reservoir and porous structure enabling passive controlled release of the drug within the tumor microenvironment. (B) Photographs showing the lateral view of the devices made of different formulations, with a ruler for size reference. (C) SEM images of the cross-sections of the devices (scale bar: 1 mm). (D) SEM images of the nanostructure of each formulation (scale bar: 20 µm). (E) Nanofibers diameter distribution for the different formulations.

implantation, offering mechanical properties that ensure stability while enabling a precisely controlled and sustained drug release governed by passive diffusion. Moreover, its favorable degradation profile eliminates the need for surgical retrieval, while its intrinsic radiopacity facilitates real-time monitoring through advanced imaging techniques.

3.4. *Sustained intratumoral release and biodistribution of α-CD40-AF790*

To evaluate real-time intratumoral drug release, we loaded α-CD40 (labeled with Alexa Fluor 790) into 1:1 and 1:4 b-NDES scaffolds and intratumorally implanted them in 4 T1 tumor-bearing mice. Fluorescent labeling enables real-time monitoring of drug in animals in a non-invasive manner via IVIS imaging. IVIS imaging across days 1, 3, 7, 10, 13, and 14 post-implantation showed local fluorescence in both formulations (Fig. 4A). The 1:4 b-NDES maintained a significantly higher signal on days 10–14 ($p < 0.05$, Fig. 4B). Ex vivo tumor imaging confirmed higher fluorescence signal in the 1:4 b-NDES group on day 14 (Fig. 4C, D) compared to 1:1 b-NDES cohort. Importantly, there was little to no fluorescent signal in systemic organs for either group, suggesting minimal off-target drug accumulation.

We selected 1:4 b-NDES for our efficacy studies as it demonstrated prolonged drug release intratumorally. Mice implanted with α-CD40-

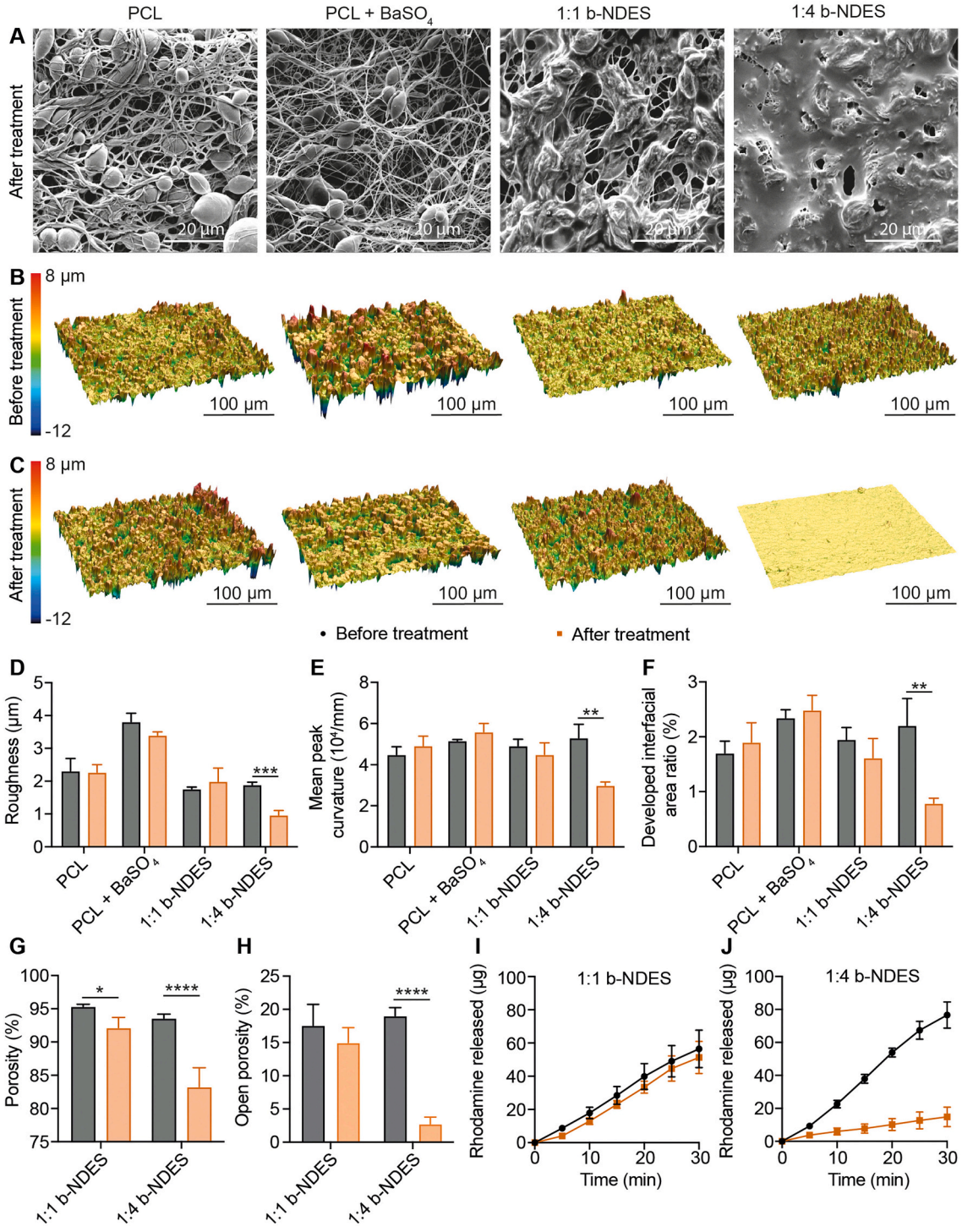

Fig. 2. Surface modification of devices by exposure to acetone vapor for 6 h, morphology, topography and in vitro release evaluation.
(A) SEM images of the device surface after 6 h of acetone vapor treatment (scale bar: 20 µm). (B) 3D surface reconstructions (scale bar: 100 µm) for all formulations before and (C) after 6 h of acetone vapor treatment. Quantitative surface descriptors, including (D) roughness, (E) peak curvature, and (F) developed interfacial area ratio, comparing the different formulations before and after 6 h of acetone vapor treatment. Device (G) porosity and (H) open porosity across formulations before and after 6 h acetone vapor treatment. Cumulative in vitro release profiles of rhodamine from (I) 1:1 b-NDES and (J) 1:4 b-NDES devices, before and after 6 h of acetone vapor treatment, showing release kinetics over time. The curves are plotted as mean ± SD, $n = 3$–5 devices per formulation. Absence of annotation indicates no significant difference, * = $p < 0.05$, ** = $p < 0.01$, *** = $p < 0.001$, **** = $p < 0.0001$.

loaded 1:4 b-NDES showed decreased tumor volume over 14 days compared to empty devices (Fig. 4E), while body weights remained stable (Fig. 4F), indicative of good tolerability and limited adverse effects. While reduced tumor growth was expected, complete tumor regression was not anticipated using α-CD40 alone, based on previous work [22]. Micro-CT scans confirmed b-NDES localization within the tumor on day 14 (Fig. 4G). Collectively, these data demonstrate that 1:4 b-NDES provides a more sustained and localized intratumoral presence of immunotherapeutic antibodies as compared to 1:1 b-NDES formulations.

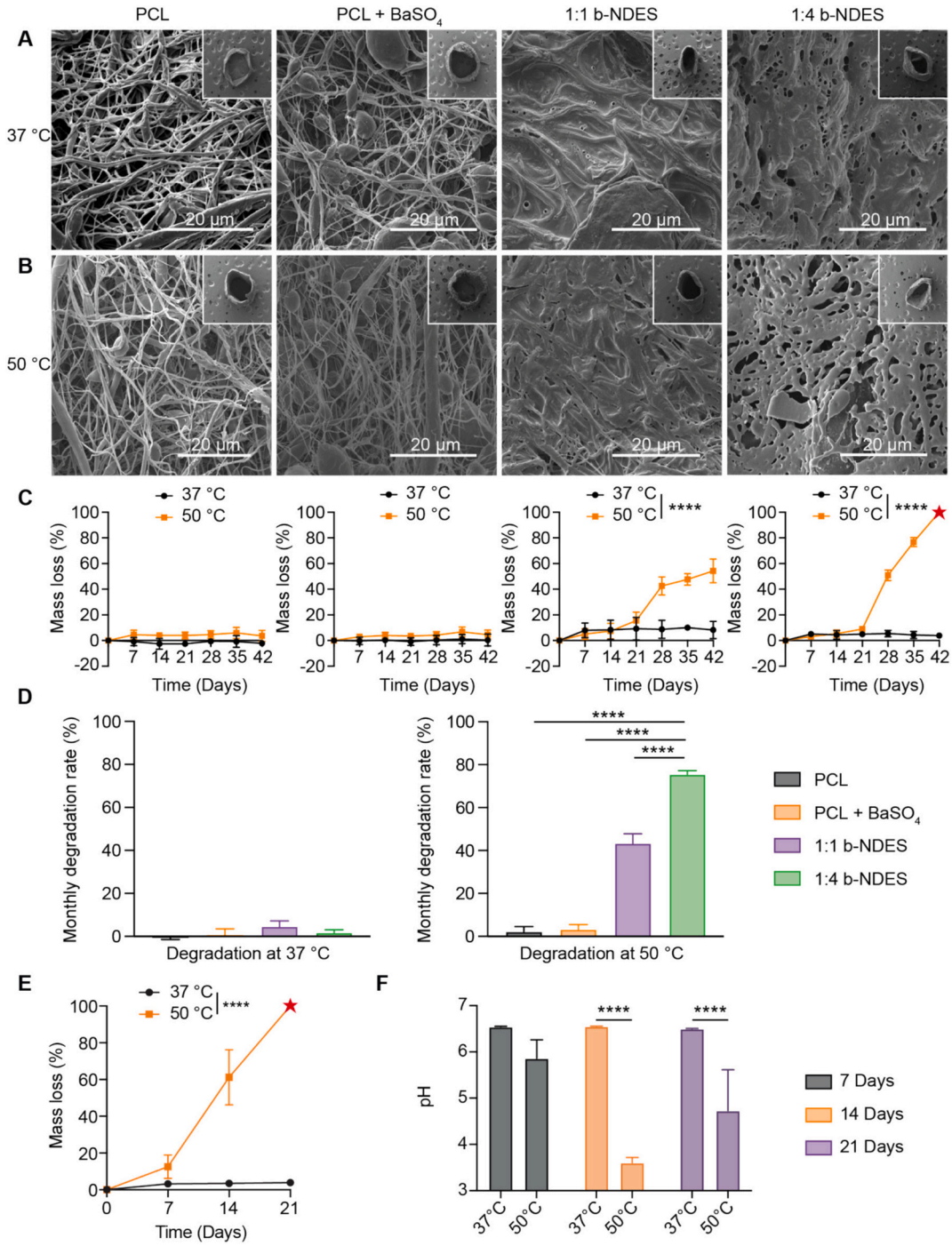

Fig. 3. Degradation tests at 37 °C and 50 °C under physiological and tumor-like (pH 6.5) conditions on devices treated with acetone vapor for 6 h.
(A) SEM images showing the nanostructure of devices from all formulations treated with acetone vapor for 6 h after degradation at 37 °C under physiological pH conditions. Insets show the corresponding cross-sections (scale bar: 20 µm). (B) SEM images showing the nanostructure of devices from all formulations treated with acetone vapor for 6 h after degradation at 50 °C under physiological pH conditions. Insets show the corresponding cross-sections (scale bar: 20 µm). (C) Mass loss profiles of devices from all formulations over time at 37 °C and 50 °C under physiological pH conditions. The star indicates time points at which the devices fragmented into unmeasurable pieces. Statistical significance between 37 °C and 50 °C refers to days 28, 35, and 42. (D) Bar graph illustrating the monthly degradation rates of all formulations at 37 °C and 50 °C under physiological pH conditions. (E) Mass loss profiles of the 1:4 b-NDES formulation treated with acetone vapor for 6 h over time at 37 °C and 50 °C under tumor-like pH conditions (pH 6.5). The star indicates time points at which the devices fragmented into unmeasurable pieces. Statistical significance between 37 °C and 50 °C refers to days 14 and 21. (F) Measurements of pH changes in the degradation medium of the 1:4 b-NDES formulation at 37 °C and 50 °C under tumor-like pH conditions. Data are presented as mean ± SD ($n = 4$). Absence of annotation indicates no statistically significant difference. * = $p < 0.05$, ** = $p < 0.01$, *** = $p < 0.001$, **** = $p < 0.0001$.

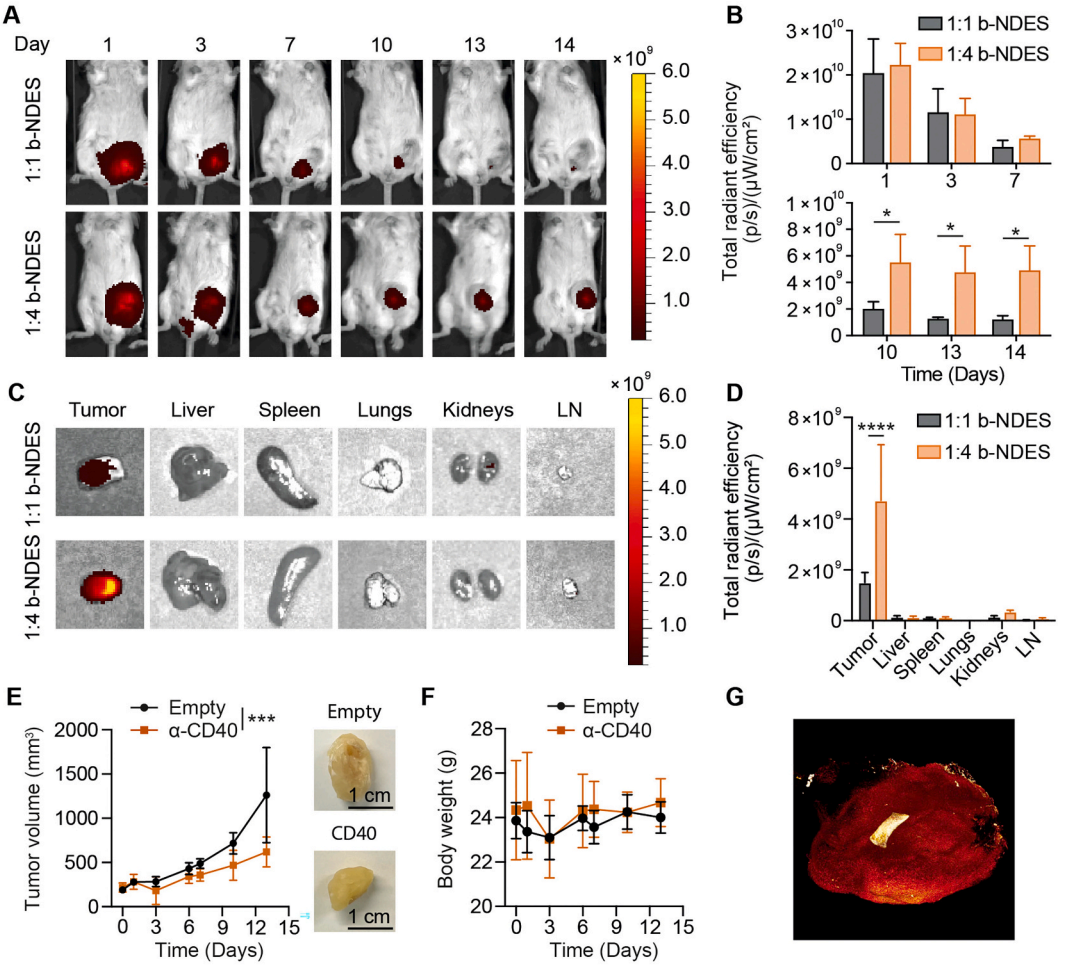

Fig. 4. In vivo and ex vivo fluorescence imaging, biodistribution, and tumor analysis in 4 T1 tumor-bearing mice implanted with b-NDES.
(A) In vivo fluorescence imaging of 4 T1 tumor-bearing mice at different time points (days 1, 3, 7, 10, 13, and 14) following implantation of 1:1 b-NDES (top row) and 1:4 b-NDES (bottom row). (B) Quantitative analysis of total radiant efficiency (p/s/cm^2/sr/μW) in the tumor region over 14 days for both 1:1 b-NDES and 1:4 b-NDES groups. (C) Ex vivo fluorescence imaging of major organs, including tumor, liver, spleen, lungs, kidneys, and lymph nodes (LN), at the study endpoint (day 14) for both 1:1 b-NDES and 1:4 b-NDES groups. (D) Quantification of total radiant efficiency in excised organs (tumor, liver, spleen, lungs, kidneys, and LN). (E) Tumor volume measurements over 14 days in mice implanted with either empty or α-CD40-loaded 1:4 b-NDES. Inset: Representative images of excised tumors from both groups on day 14. (F) Body weight monitoring of mice implanted with empty or α-CD40-loaded devices over 14 days. (G) CT imaging of excised tumors on day 14, showing the presence of the implanted device within the tumor. Data are presented as mean ± SD, $n = 3$. Absence of annotation indicates no significant difference, * = $p < 0.05$, ** = $p < 0.01$, *** = $p < 0.001$, **** = $p < 0.0001$.

3.5. Local tumor control by radiation and using b-NDES to deliver CD40 agonists, STING activators

Radiotherapy plus immunostimulatory agents, particularly CD40 agonists and STING activators, can synergistically enhance antitumor immune responses [39]. Radiotherapy induces immunogenic cell death to improve tumor antigen presentation, while CD40 agonist promotes dendritic cell maturation and subsequent T-cell activation [31,40]. Concurrently, STING pathway activation amplifies innate immune responses by triggering the production of Type I Interferons, further strengthening tumor-directed immune activity [30]. However, monotherapies based on these mechanisms often yield limited efficacy, and systemic combination treatments are frequently constrained by off-target toxicities, limiting their clinical applicability. Consistent with our previous finding [22], CD40 agonist monotherapy provided partial tumor control with modest tumor volume reduction and limited overall therapeutic efficacy (Fig. 4E). This highlights the need for combinatorial approaches to enhance efficacy and achieve more robust tumor suppression.

To overcome these limitations, we used a localized immunotherapeutic strategy by integrating radiotherapy with b-NDES for sustained intratumoral delivery of α-CD40 and STINGa (Fig. 5A). We administered 8 Gy fractions on the 4 T1 tumor over three consecutive days, then intratumorally implanted b-NDES loaded with α-CD40 and STINGa, whose in vitro release rates were 23.75 ± 11.24 μg/day for α-CD40 and 63.71 ± 16.84 μg/day for polymeric STING agonist (STINGa, corresponding to 3.50 ± 0.93 μg/day of active STING) (Fig. S2A—B). Tumors receiving this triple regimen (Rad+α-CD40 + STINGa) demonstrated greater growth inhibition versus monotherapies or α-CD40 + STINGa without radiation ($p < 0.001$, Fig. 5B) and with significantly more uniform regression across individual tumors (Fig. 5C). Three out of five mice achieved complete remission of the orthotopic tumors (Fig. 5D). Although mice ultimately succumbed to spontaneous lung metastases (Fig. S2C–E), the combination of radiotherapy with α-CD40 and STINGa significantly extended survival compared to our previous regimen of radiotherapy, α-CD40 and α-PD-L1, highlighting the improved therapeutic benefit of this approach [25].

To evaluate therapeutic efficacy and associated immune responses, tumor burden, intratumoral immune composition, and systemic cytokines were analyzed following 7 days of intratumoral treatment. The 7-day time point was selected to ensure sufficient tumor mass remained for immune profiling analysis. Gross inspection and tumor weight

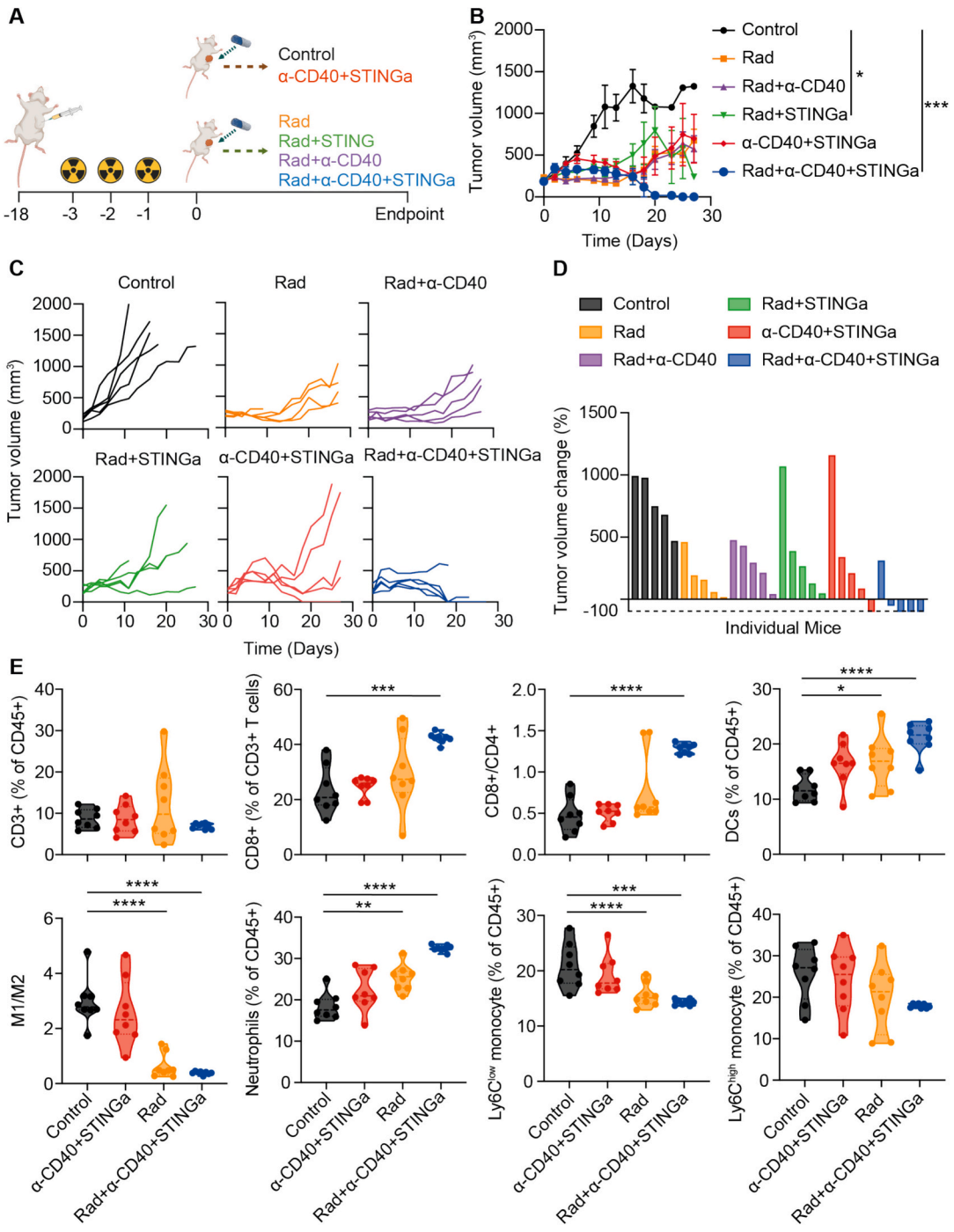

Fig. 5. Therapeutic efficacy and immunological mechanisms of radiation, CD40 agonist antibody, and a STING agonist.
(A) Schematic representation of the experimental timeline. Mice were treated with or without radiation, followed by localized intratumoral delivery of α-CD40 and/or STINGa via b-NDES. (B) Tumor growth curves over time for each treatment group. Data are presented as mean ± SEM, $n = 5$. (C) Individual tumor growth trajectories for each treatment group. (D) Tumor volume change (%) in individual mice across different treatment groups. (E) Flow cytometry analysis of tumor-infiltrating immune cell populations at day 7 following the different treatments. Violin plots show the frequency of $CD3^+$ T cells, $CD8^+$ T cells (as a percentage of $CD3^+$ cells), $CD8^+/CD4^+$ ratio, dendritic cells (DCs), M1/M2 ratio, neutrophils, $Ly6C^{low}$ monocytes, and $Ly6C^{high}$ monocytes, all expressed as a percentage of $CD45^+$ cells. ($n = 8$). Absence of annotation indicates no significant difference, * = $p < 0.05$, ** = $p < 0.01$, *** = $p < 0.001$, **** = $p < 0.0001$.

measurements demonstrated that radiation-containing regimens (Rad and Rad+αCD40 + STING) produced comparable early tumor debulking relative to control and αCD40 + STING alone at Day 7 (Fig. S2F–G). Despite similar early tumor burden, radiation-only tumors began to regrow around Day 10, whereas Rad+αCD40 + STING maintained sustained tumor control (Fig. 5C).

Flow cytometric analysis at Day 7 (Fig. 5E) revealed that although total $CD3^+$ T-cell frequencies among $CD45^+$ leukocytes were unchanged, the Rad+α-CD40 + STING regimen induced pronounced remodeling within the T-cell compartment. This group exhibited the highest proportion of $CD8^+$ T cells among $CD3^+$ lymphocytes and the greatest $CD8^+$:$CD4^+$ ratio, indicating preferential enrichment of cytotoxic T cells. Dendritic cells were also significantly increased in the combination group, consistent with enhanced antigen-presenting

capacity within the tumor microenvironment.

Radiation-containing regimens were associated with increased neutrophil infiltration, with the highest levels observed in the Rad+α-CD40 + STING group, consistent with an acute post-irradiation inflammatory response at this early timepoint. In contrast, Ly6C^{high} inflammatory monocytes were significantly reduced in radiation-treated tumors, particularly in the combination arm. Macrophage polarization, assessed using an M1/M2 index defined by the ratio of CD86^{+} (M1-like) to MR^{+} (M2-like) tumor-associated macrophages, was decreased in radiation-containing groups and lowest in the Rad+α-CD40 + STING group, indicating a relative enrichment of MR^{+} TAM phenotypes at Day 7. These myeloid changes are consistent with an early inflammatory and tissue-remodeling phase occurring during the active intratumoral drug-release period.

To assess whether localized immune modulation was associated with systemic inflammatory signals, circulating cytokines and chemokines were quantified by Luminex analysis (Fig. S2H). Administration of α-CD40 + STING agonists increased serum IL-6 and IL-10 levels,

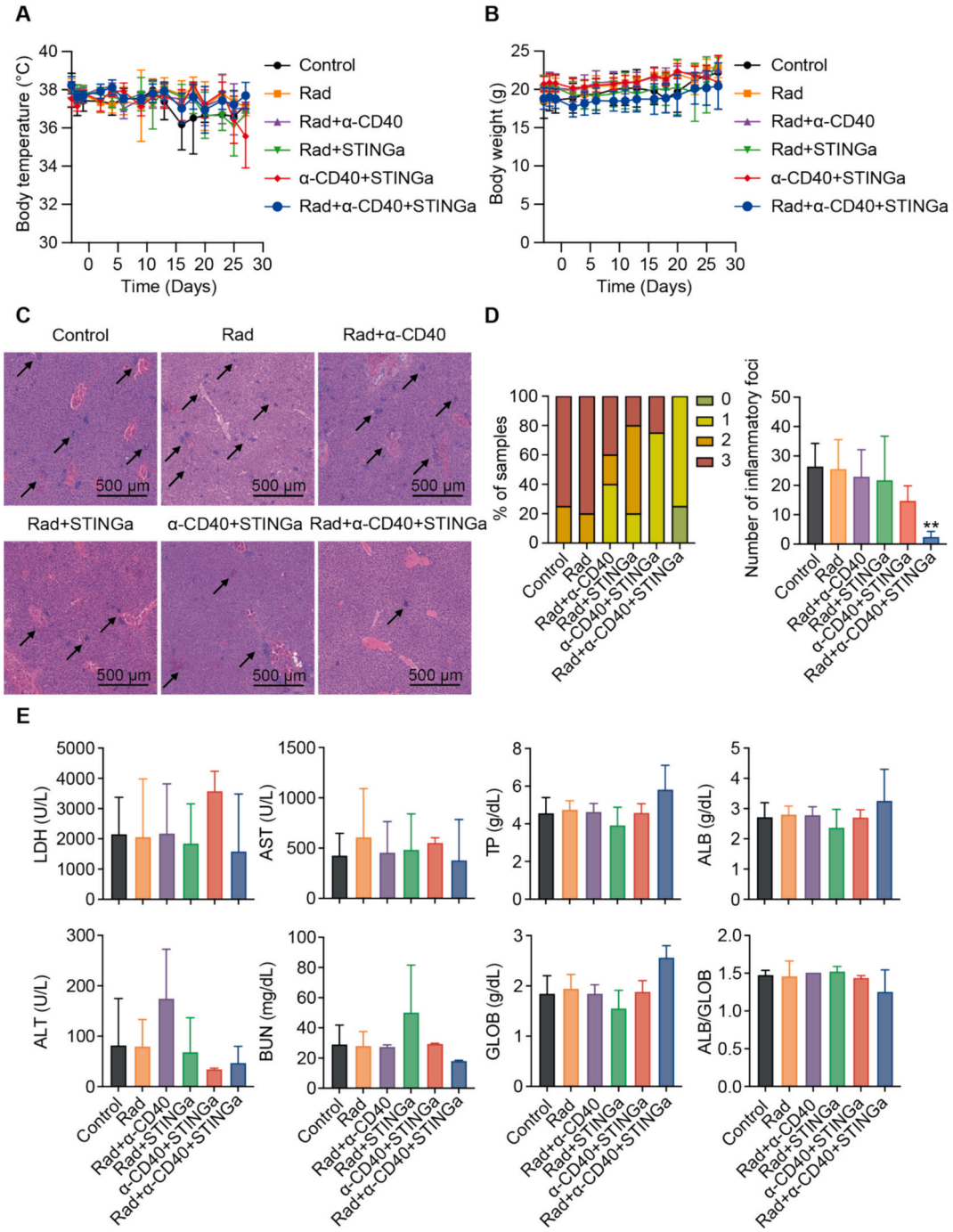

Fig. 6. Physiological, liver inflammation and organ functionality assessments.
(A) Body temperature and (B) body weight measurements recorded over time across different treatment groups. Data are presented as mean ± SD, n = 5. (C) Representative histopathological images of liver tissues from different treatment groups (scale bar: 500 μm). (D) Liver inflammation scoring based on histopathological assessment. (E) Blood chemistry analysis of the key indicators of hepatic, renal, and muscular function: lactate dehydrogenase (LDH), aspartate aminotransferase (AST), total protein (TP), albumin (ALB), alanine aminotransferase (ALT), blood urea nitrogen (BUN), globulins (GLOB), and the albumin/globulin ratio (ALB/GLOB). Data are presented as mean ± SD, n = 2–5. Absence of annotation indicates no significant difference, ** = $p < 0.01$.

indicating detectable systemic immune signaling following intratumoral delivery. Importantly, incorporation of radiation did not further amplify these responses; IL-10 levels were significantly attenuated in the Rad+α-CD40 + STING group compared with α-CD40 + STING alone. Serum IP-10 (CXCL10) and TNF-α levels remained comparable across treatment groups, indicating that the three-component combination elicited systemic immune signaling without inducing broad systemic inflammatory cytokine release.

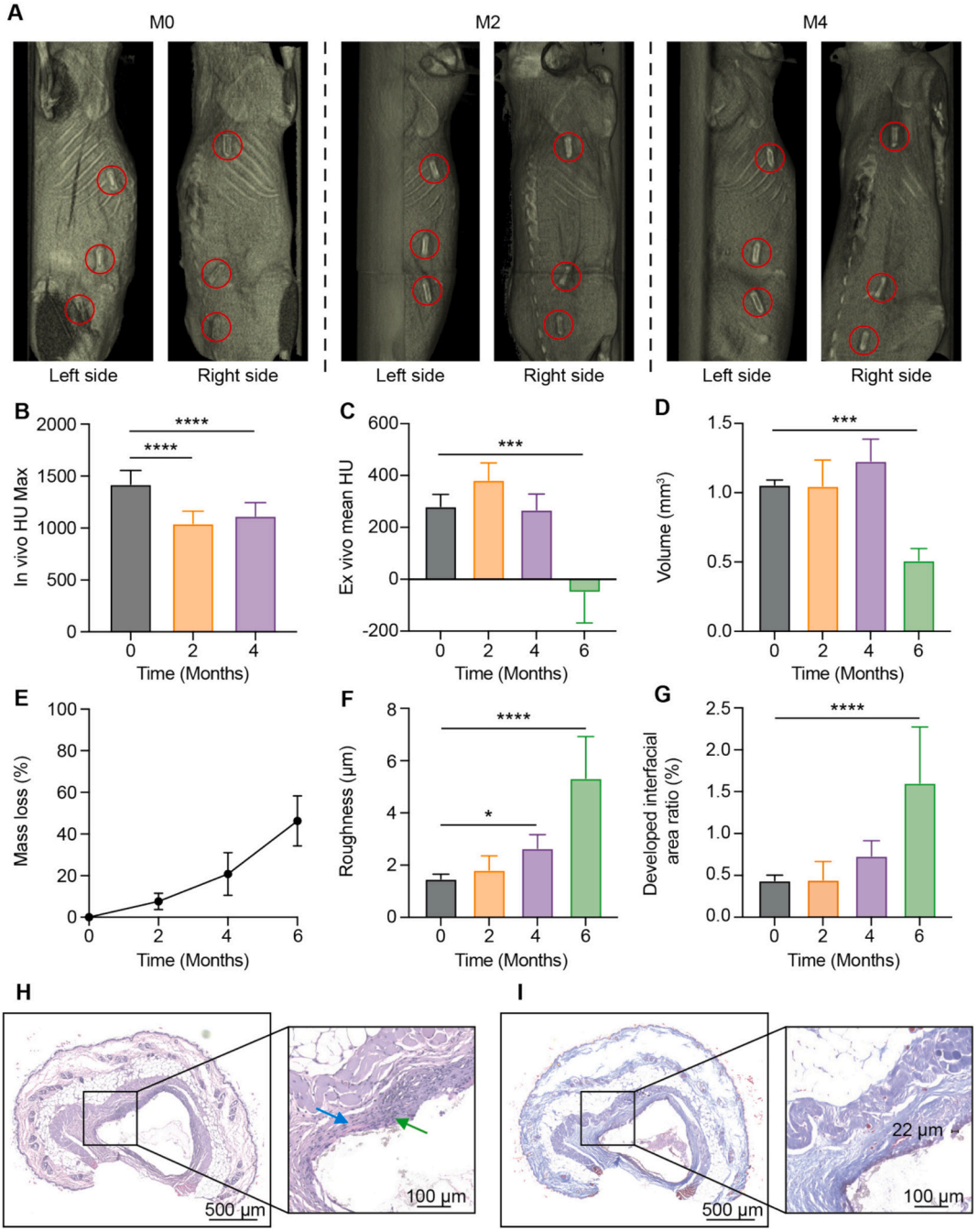

Fig. 7. In vivo degradation profile and biocompatibility of b-NDES following subcutaneous implantation in mice.
(A) Representative in vivo CT images showing device implantation sites (red circles) at month 0 (M0), month 2 (M2), and month 4 (M4) on the left and right sides. CT-based quantitative analysis of device radiopacity and structural evolution over time. Device radiopacity is conferred by $BaSO_4$ incorporated within the polymeric matrix: (B) quantification of maximum Hounsfield Unit (HU Max) values measured in vivo from implanted devices at different time points ($n = 12$); (C) quantification of mean HU values and (D) device volume measured ex vivo from explanted devices at corresponding time points ($n = 4$). (E) Device mass loss percentage as a function of time ($n = 9$–12). (F) Surface roughness of the devices measured over time. (G) Developed interfacial area ratio of the devices as a function of time (n = 4). (H) Representative H&*E*-stained histological section of the implantation site at month 4, showing a low-magnification overview with the corresponding higher-magnification inset (scale bars: 500 µm and 100 µm, respectively). The blue arrow indicates a narrow band of fibrous connective tissue surrounding the implantation site. The green arrow highlights a mild–moderate inflammatory cell infiltration, composed primarily of polymorphonuclear cells, lymphocytes, and macrophages ($n = 3$). (I) Representative Masson's Trichrome–stained histological section of the implantation site at month 4, with low-magnification overview and corresponding higher-magnification inset (scale bars: 500 µm and 100 µm, respectively) (n = 3). Data are presented as mean ± SD. Absence of annotation indicates no statistically significant difference. * $p \leq 0.05$, *** $p \leq 0.001$, **** $p \leq 0.0001$.

Together, these data show that b-NDES–mediated intratumoral delivery of CD40 agonist and STING activator converts radiation-induced transient tumor debulking into durable local control, coinciding with coordinated intratumoral immune remodeling during drug release and minimal systemic cytokine induction.

3.6. Systemic tolerability, liver pathology and blood chemistry

Throughout treatment, mice maintained stable body temperature (Fig. 6A) and weight (Fig. 6B), indicating the absence of acute systemic inflammatory responses. This suggests that the localized nature of the therapeutic strategy effectively minimizes systemic adverse effects, thereby improving treatment safety. Histological scoring of liver sections showed no severe adverse pathology (Fig. 6C-D). Blood chemistry profiles remained within normal ranges across all groups, with no abnormalities in hepatic, renal, or muscular markers (Fig. 6E). By confining immunostimulatory delivery to the tumor site, systemic toxicity was minimized, underscoring the value of localized b-NDES-mediated therapy.

3.7. In vivo subcutaneous degradation profile and biocompatibility of b-NDES

The in vivo degradation profile of b-NDES was investigated following subcutaneous implantation of the devices in mice. This approach avoids the temporal limitations of tumor-bearing models, where studies are terminated within a short timeframe due to lethal tumor progression or the total resolution of the tumor mass in responding cohorts. Device degradation was longitudinally evaluated using CT imaging, mass loss measurements, and surface topographical analyses. CT reconstructions showed that the device remained detectable up to 4 months post-implantation, while the radiopaque signal progressively decreased over time, consistent with gradual material loss (Fig. 7A–B). These findings were confirmed by ex vivo CT analysis of explanted devices, where progressive loss of the $BaSO_4$-containing matrix was associated with reduced signal intensity and a concomitant decrease in device volume over time (Fig. 7C–D). The negative HU observed at Month 6 likely reflects advanced degradation with reduced radiopaque content and the presence of residual low-density tissue associated with the explanted device. Quantitative analysis confirmed a continuous reduction in device mass, with an overall mass loss of $46.32 \pm 12.01\%$ at 6 months (Fig. 7E). In parallel, surface analysis revealed increased surface roughness and morphological complexity over time (Fig. 7F-G), in agreement with progressive material degradation.

H&E histopathological evaluation was performed 4 months post-implantation to assess the presence and extent of inflammatory cell infiltration and necrosis around the implant site (Fig. 7H; Tables 1 and 2). Infiltrates were predominantly composed of polymorphonuclear cells, lymphocytes, and macrophages and were observed at mild to moderate levels. The samples exhibited an average reactive grade score of 6.67 ± 0.58 (Table 3), corresponding to a slight tissue reaction. Masson's Trichrome staining revealed the presence of a thin and well-defined fibrotic capsule encapsulating the implant, with an average thickness of 22.57 ± 3.03 μm (Fig. 7I). Consistent with the H&E findings, the local tissue reactivity was classified as slight.

Overall, the observed degradation kinetics and favorable tissue response indicate a well-integrated device undergoing sustained in vivo resorption.

4. Conclusion

b-NDES is a biodegradable and biocompatible intratumoral drug delivery platform that enables controlled and sustained release of immunotherapeutics into the tumor microenvironment while minimizing systemic dissemination. Device radiopacity allows real-time CT monitoring of its localization and structural stability throughout its gradual degradation, which ultimately eliminates the need for surgical removal. The combination of radiotherapy and intratumoral release of immunostimulatory agents via b-NDES elicited a potent local antitumor immune response, resulting in primary tumor eradication without evidence of systemic toxicity. Overall, b-NDES is an effective and safe platform for intratumoral immunotherapy delivery. However, future studies delivering combination immunotherapeutic regimens are required to assess the capacity of b-NDES to generate a more potent systemic antitumor immune response.

CRediT authorship contribution statement

Francesco Manfredi: Writing – review & editing, Writing – original draft, Visualization, Validation, Software, Methodology, Formal analysis, Data curation, Conceptualization. **Jingyi Wang:** Writing – review & editing, Writing – original draft, Visualization, Validation, Supervision, Software, Methodology, Formal analysis, Data curation, Conceptualization. **Eleonora Molinari:** Visualization, Validation, Software, Methodology, Formal analysis, Data curation, Conceptualization. **Robin Vander Pol:** Methodology, Data curation. **Casey Lewis:** Software, Methodology. **Xinyi Peng:** Methodology. **Nicola Di Trani:** Validation, Supervision. **Marco Maria Paci:** Methodology. **Danilo Settis:** Methodology. **Madison Alexandra Deeson:** Methodology. **Yongbin Liu:** Writing – review & editing. **Andrew Badachhape:** Software. **Laxman Devkota:** Software. **Michael Ittmann:** Methodology. **Mahmoud Elsayad:** Formal analysis. **Dinh Chuong Nguyen:** Methodology. **Simbarashe Jokonya:** Methodology. **Patrick S. Stayton:** Methodology. **Corrine Ying Xuan Chua:** Writing – review & editing, Supervision, Resources, Project administration, Investigation, Funding acquisition. **Alessandro Grattoni:** Writing – review & editing, Supervision, Resources, Investigation, Funding acquisition.

Acknowledgements

This work is supported by the Houston Methodist Research Institute, the Nancy Owens Breast Cancer Foundation (A.G. and C.C.Y.X.) the U Foundation (C.C.Y.X.), and the National Institutes of Health/National Cancer Institute grant R01CA257563 (P.S·S). We thank Dr. Jianhua (James) Gu from the Electron Microscopy Core, Dr. Feng Li from the Translational Imaging - Preclinical Imaging (Small Animal) Core, Dr. Yuelan Ren from the Research Pathology Core, and Drs. Ramiro Pino and Devin Olek from the Department of Radiation Oncology at the Houston Methodist Research Institute for their valuable support for the murine radiation study. We acknowledge the Texas Children's Hospital Small Animal Imaging Facility (SAIF) for micro-CT imaging. A.G. is a co-founder of Continuity Biosciences.

Appendix A. Supplementary data

Supplementary data to this article can be found online at https://doi.org/10.1016/j.jconrel.2026.115004.

Data availability

Data will be made available on request.

References

[1] P. Garg, S. Pareek, P. Kulkarni, D. Horne, R. Salgia, S.S. Singhal, Next-generation immunotherapy: advancing clinical applications in cancer treatment, J. Clin. Med. 13 (21) (2024) 6537, https://doi.org/10.3390/jcm13216537.

[2] Y. Zhang, Z. Zhang, The history and advances in cancer immunotherapy: understanding the characteristics of tumor-infiltrating immune cells and their therapeutic implications, Cell. Mol. Immunol. 17 (8) (2020) 807–821, https://doi.org/10.1038/s41423-020-0488-6.

[3] C.Y.X. Chua, J. Ho, S. Demaria, M. Ferrari, A. Grattoni, Emerging technologies for local cancer treatment, Adv. Ther. 3 (9) (2020) 2000027, https://doi.org/10.1002/adtp.202000027.

[4] M.W. Dewhirst, T.W. Secomb, Transport of drugs from blood vessels to tumour tissue, Nat. Rev. Cancer 17 (12) (2017) 738–750, https://doi.org/10.1038/nrc.2017.93.

[5] T. Stylianopoulos, L.L. Munn, R.K. Jain, Reengineering the physical microenvironment of tumors to improve drug delivery and efficacy: from mathematical modeling to bench to bedside, Trends Cancer 4 (4) (2018) 292–319, https://doi.org/10.1016/j.trecan.2018.02.005.

[6] S. Nizzero, A. Ziemys, M. Ferrari, Transport barriers and oncophysics in cancer treatment, Trends Cancer 4 (4) (2018) 277–280, https://doi.org/10.1016/j.trecan.2018.02.008.

[7] N. Chhabra, J. Kennedy, A review of cancer immunotherapy toxicity: immune checkpoint inhibitors, J. Med. Toxicol. 17 (4) (2021) 411–424, https://doi.org/10.1007/s13181-021-00833-8.

[8] J.M. Michot, C. Bigenwald, S. Champiat, et al., Immune-related adverse events with immune checkpoint blockade: a comprehensive review, Eur. J. Cancer 54 (2016) 139–148, https://doi.org/10.1016/j.ejca.2015.11.016.

[9] T.Z. Horvat, N.G. Adel, T.O. Dang, et al., Immune-related adverse events, need for systemic immunosuppression, and effects on survival and time to treatment failure in patients with melanoma treated with Ipilimumab at Memorial Sloan Kettering Cancer Center, J. Clin. Oncol. 33 (28) (2015) 3193–3198, https://doi.org/10.1200/JCO.2015.60.8448.

[10] G.R. Khosravi, S. Mostafavi, S. Bastan, N. Ebrahimi, R.S. Gharibvand, N. Eskandari, Immunologic tumor microenvironment modulators for turning cold tumors hot, Cancer Commun. 44 (5) (2024) 521–553, https://doi.org/10.1002/cac2.12539.

[11] M. Skalickova, K. Hadrava Vanova, O. Uher, et al., Injecting hope: the potential of intratumoral immunotherapy for locally advanced and metastatic cancer, Front. Immunol. 15 (2025), https://doi.org/10.3389/fimmu.2024.1479483.

[12] S.M. Mantooth, Y. Abdou, A.R. Saez-Ibañez, S. Upadhaya, D.A. Zaharoff, Intratumoral delivery of immunotherapy to treat breast cancer: current development in clinical and preclinical studies, Front. Immunol. 15 (2024) 1385484, https://doi.org/10.3389/fimmu.2024.1385484.

[13] A. Marabelle, L. Tselikas, T. de Baere, R. Houot, Intratumoral immunotherapy: using the tumor as the remedy, Ann. Oncol. 28 (suppl_12) (2017) xii33–xii43, https://doi.org/10.1093/annonc/mdx683.

[14] A. Som, J.G. Rosenboom, A. Chandler, R.A. Sheth, E. Wehrenberg-Klee, Image-guided intratumoral immunotherapy: developing a clinically practical technology, Adv. Drug Deliv. Rev. 189 (2022) 114505, https://doi.org/10.1016/j.addr.2022.114505.

[15] R.A. Sheth, R. Murthy, D.S. Hong, et al., Assessment of image-guided intratumoral delivery of Immunotherapeutics in patients with cancer, JAMA Netw. Open 3 (7) (2020) e207911, https://doi.org/10.1001/jamanetworkopen.2020.7911.

[16] A. Gagliardi, E. Giuliano, E. Venkateswararao, et al., Biodegradable polymeric nanoparticles for drug delivery to solid tumors, Front. Pharmacol. 12 (2021) 601626, https://doi.org/10.3389/fphar.2021.601626.

[17] A. Raeisi, F. Farjadian, Commercial hydrogel product for drug delivery based on route of administration, Front. Chem. 12 (2024), https://doi.org/10.3389/fchem.2024.1336717.

[18] Q. Chen, L. Yuan, W.C. Chou, et al., Meta-analysis of nanoparticle distribution in tumors and major organs in tumor-bearing mice, ACS Nano 17 (20) (2023) 19810–19831, https://doi.org/10.1021/acsnano.3c04037.

[19] Z. (Georgia) Chen, Small-molecule delivery by nanoparticles for anticancer therapy, Trends Mol. Med. 16 (12) (2010) 594–602, https://doi.org/10.1016/j.molmed.2010.08.001.

[20] S.M. Mantooth, J.M. Green, W.D. Green, et al., An injectable hydrogel enhances intratumoral retention and antitumor efficacy of cytokine immunotherapy in murine triple negative breast tumor models, J. Control. Release 383 (2025) 113761, https://doi.org/10.1016/j.jconrel.2025.113761.

[21] R.L. Hood, G. Bruno, P. Jain, et al., Nanochannel implants for minimally-invasive insertion and intratumoral delivery, J. Biomed. Nanotechnol. 12 (10) (2016) 1907–1915, https://doi.org/10.1166/jbn.2016.2288.

[22] C.Y.X. Chua, P. Jain, A. Susnjar, et al., Nanofluidic drug-eluting seed for sustained intratumoral immunotherapy in triple negative breast cancer, J. Control. Release 285 (2018) 23–34, https://doi.org/10.1016/j.jconrel.2018.06.035.

[23] J. Ho, A. Susnjar, J. Rhudy, et al., Localizing radioimmunotherapy via nanochannel device for sustained intratumoral drug delivery for solid tumor treatment, J. Clin. Oncol. 37 (8_suppl) (2019) 37, https://doi.org/10.1200/JCO.2019.37.8_suppl.37.

[24] C.Y.X. Chua, J. Ho, A. Susnjar, et al., Intratumoral nanofluidic system for enhancing tumor biodistribution of agonist CD40 antibody, Adv. Ther. 3 (10) (2020) 2000055, https://doi.org/10.1002/adtp.202000055.

[25] H.C. Liu, D.I. Viswanath, F. Pesaresi, et al., Potentiating antitumor efficacy through radiation and sustained intratumoral delivery of anti-CD40 and anti-PDL1, Int. J. Radiat. Oncol. Biol. Phys. 110 (2) (2021) 492–506, https://doi.org/10.1016/j.ijrobp.2020.07.2326.

[26] H.C. Liu, D. Davila Gonzalez, D.I. Viswanath, et al., Sustained Intratumoral Administration of Agonist CD40 antibody overcomes immunosuppressive tumor microenvironment in pancreatic cancer, Adv. Sci. Weinh. Baden-Wurtt. Ger. 10 (9) (2023) e2206873, https://doi.org/10.1002/advs.202206873.

[27] H.C. Liu, S. Capuani, A.A. Badachhape, et al., Intratumoral nanofluidic system enhanced tumor biodistribution of PD-L1 antibody in triple-negative breast cancer, Bioeng. Transl. Med. 8 (6) (2023) e10594, https://doi.org/10.1002/btm2.10594.

[28] H.C. Liu, N. Di Trani, M. Conte, et al., Nanofluidic delivery implant sustains localization and maximizes efficacy of intratumoral immunotherapy, Nano Today 56 (2024) 102258, https://doi.org/10.1016/j.nantod.2024.102258.

[29] D.C. Nguyen, K. Song, S. Jokonya, et al., Mannosylated STING agonist drugamers for dendritic cell-mediated cancer immunotherapy, ACS Cent. Sci. 10 (3) (2024) 666–675, https://doi.org/10.1021/acscentsci.3c01310.

[30] Y. Wang, J. Luo, A. Alu, X. Han, Y. Wei, X. Wei, cGAS-STING pathway in cancer biotherapy, Mol. Cancer 19 (1) (2020) 136, https://doi.org/10.1186/s12943-020-01247-w.

[31] R.H. Vonderheide, CD40 agonist antibodies in cancer immunotherapy, Annu. Rev. Med. 71 (2020) 47–58, https://doi.org/10.1146/annurev-med-062518-045435.

[32] P.O. Gendron, F. Avaltroni, K.J. Wilkinson, Diffusion coefficients of several rhodamine derivatives as determined by pulsed field gradient–nuclear magnetic resonance and fluorescence correlation spectroscopy, J. Fluoresc. 18 (6) (2008) 1093–1101, https://doi.org/10.1007/s10895-008-0357-7.

[33] W.J. Kim, O. Campanella, D.R. Heldman, Predicting the performance of direct contact membrane distillation (DCMD): mathematical determination of appropriate tortuosity based on porosity, J. Food Eng. 294 (2021) 110400, https://doi.org/10.1016/j.jfoodeng.2020.110400.

[34] N. Cheng, R. Watkins-Schulz, R.D. Junkins, et al., A nanoparticle-incorporated STING activator enhances antitumor immunity in PD-L1–insensitive models of triple-negative breast cancer, JCI Insight 3 (22) (2018) e120638, https://doi.org/10.1172/jci.insight.120638.

[35] S.H. Youssef, S. Kim, R. Khetan, F. Afinjuomo, Y. Song, S. Garg, The development of 5-fluorouracil biodegradable implants: a comparative study of PCL/PLGA blends, J. Drug Delivery Sci. Technol. 81 (2023) 104300, https://doi.org/10.1016/j.jddst.2023.104300.

[36] Y. Li, J. Zhu, H. Cheng, et al., Developments of advanced electrospinning techniques: a critical review, Adv. Mater. Technol. 6 (11) (2021) 2100410, https://doi.org/10.1002/admt.202100410.

[37] T.K. Dash, V.B. Konkimalla, Poly-ϵ-caprolactone based formulations for drug delivery and tissue engineering: a review, J. Control. Release 158 (1) (2012) 15–33, https://doi.org/10.1016/j.jconrel.2011.09.064.

[38] J. Walker, J. Albert, D. Liang, et al., In vitro degradation and erosion behavior of commercial PLGAs used for controlled drug delivery, Drug Deliv. Transl. Res. 13 (1) (2023) 237–251, https://doi.org/10.1007/s13346-022-01177-8.

[39] E.C. Ko, S.C. Formenti, Radiation therapy to enhance tumor immunotherapy: a novel application for an established modality, Int. J. Radiat. Biol. 95 (7) (2019) 936–939, https://doi.org/10.1080/09553002.2019.1623429.

[40] C. Hennequin, Y. Belkacémi, C. Bourgier, et al., Radiotherapy of breast cancer, Cancer Radiother J Soc Francaise Radiother Oncol. 26 (1–2) (2022) 221–230, https://doi.org/10.1016/j.canrad.2021.11.013.